Journal of
Composites Science

MDPI

Article

Computational Study of Non-Porous Auxetic Plates with Diamond Shape Inclusions

Arash Afshar [1,*] and Hamed Rezvanpour [2]

[1] School of Engineering, Mercer University, Macon, GA 31207, USA
[2] School of Automotive Engineering, Iran University of Science and Technology, Tehran 13114-16846, Iran; hamed.rzp@gmail.com
* Correspondence: afshar_a@mercer.edu; Tel.: +1-478-301-2421

Abstract: Creating non-porous structures that offer auxetic behavior can have a variety of industrial applications, especially when the porosity impairs the functionality of the auxetic structures. This study presents the design and finite element analysis of architected bi-material auxetic plates consisting of repeating unit cells that comprise rigid rotary units and soft inclusions. The change in the design parameters of unit cells produces a variety of mechanical properties, such as different levels of Poisson's ratio and stiffness for the architected plates that can result in specific static or dynamic responses. The natural frequencies and deflection under uniform lateral loading of the architected plates with clamped boundary conditions were investigated. Furthermore, the effectiveness of the homogenization technique based on the mechanical properties obtained from finite element analysis in predicting the dynamic and static response of the architected plate was also studied.

Keywords: non-porous; bi-material; auxetic plate; design parameter; cellular structure; static response; dynamic response

Citation: Afshar, A.; Rezvanpour, H. Computational Study of Non-Porous Auxetic Plates with Diamond Shape Inclusions. *J. Compos. Sci.* **2022**, *6*, 192. https://doi.org/10.3390/jcs6070192

Academic Editor: Francesco Tornabene

Received: 16 May 2022
Accepted: 29 June 2022
Published: 1 July 2022

1. Introduction

Poisson's ratio is a dimensionless measure that describes the deformation of a material in the perpendicular direction of the loading [1]. Materials with negative Poisson's ratio (NPR) properties are usually referred to as auxetic materials [2,3]. The term auxetic in the scientific literature was introduced by Evans [4]. Auxetic materials have been known for more than 150 years, and in 1882, a study revealed that they could be found in nature as iron pyrite nanocrystals with an estimated Poisson's ratio of $-1/7$ [5]. There are other natural examples such as α-cristobalite, cow teat skin, pyrolytic graphite, polymorphic silicones, zeolites, silicates, and crystal cadmium [6]. The first artificial auxetic material was synthesized as a foam shape in 1987 by Lakes [7], which was followed by a significant number of studies to develop materials with NPR properties along with cost-effectiveness and manufacturing controllability [8–18].

Based on the classical theory of elasticity, all three-dimensional isotropic materials can have a Poisson's ratio ranging from -1 to 0.5, while for two-dimensional isotropic materials, this ratio is between -1 to 1 [19,20]. Materials that show a negative Poisson's ratio in all directions are called auxetic or completely auxetic materials [21,22]. On the other hand, some materials behave as auxetic in some directions and non-auxetic in others, and are known as partially auxetic materials [23,24].

One of the first mechanical structures with auxetic behavior was proposed by Almgren [25] and the first 2D molecular models (spontaneously forming auxetic phases) were studied by Wojciechowski [19]. Auxetic structures can provide a variety of improved properties such as high shear and overall stiffness [26–28], fracture toughness [29], and indentation resistance [9]. In addition, the damping capacity of auxetic structures [10], their sound absorption [30,31], and crashworthiness [32] were also found to be enhanced

compared to conventional materials. These remarkable properties made auxetic materials a perfect choice for some engineering applications, including biomedical materials [24], energy absorbers [33], and applications in the automotive [34] and military and aerospace industries [35].

Conventional materials show a saddle shape (anticlastic curvature) when a bending force acts on them due to the transverse shrinkage. However, auxetic materials demonstrate a dome shape (synclastic curvature) [7,27] in the transverse direction, which has the same curve trend as the bending direction. Therefore, the synclastic curvature property makes an auxetic material a better fit for creating structures with complex curvatures without excessive machining and forcing materials to take up a specific shape (e.g., conical shape) that could result in possible damage [36,37].

The auxetic effect is not only an intrinsic property of the material, but can also be achieved by designing the structure and the deformation mechanism [38]. Auxetic materials can have different structural shapes, such as chiral structures, fibril/nodule structures, Miura-folded structures, buckling-induced structures, helical auxetic yarn structures, and crumpled structures [39]. The re-entrant structures that comprise rigid rotary units with square or triangle inclusions can also exhibit a negative Poisson's ratio [40–45]. The unit cells with orthogonal geometrical shapes can only offer an auxetic behavior in certain symmetry axes. However, it has been shown that inclusions in the form of re-entrant triangles can offer an NPR effect along all symmetry axes due to the nonorthogonal symmetrical feature of the structure [46]. The auxetic behavior both in tension and compression was observed in structural sheets containing either diamond- or star-shaped perforations [47]. The auxetic behavior of the re-entrant structures at the molecular level has also received great attention [48,49].

Manufactured auxetic materials, like other periodic structures, usually possess some porosities in their structures [50–52], since the formation of the porosity is crucial to the auxetic properties. The porose auxetic structures typically contain sharp corners or wedge angles. In regards to fracture mechanics, the stress concentration around the holes and corners may compromise the structural integrity under loading conditions [53,54]. This phenomenon may limit the scope of application of the auxetic material. Having porosity in the structure may also cause other disadvantages, such as exposing the interior part of the structure to erosive and corrosive environments that can damage the structure and impair its function [55–58]. To eliminate the porosity, some continuous auxetic structures are proposed in the literature, such as smooth curve sheets [59], dimpled sheets [60], re-entrant hollow skeletons [61], wrinkled paper sheets [18], and origami sheets [62]. However, all of these structures are made from single materials. Creating structures from different materials can offer some benefits, such as producing certain structural properties at exact locations and tailoring them for specific applications [63].

Numerous studies have found analytical models for calculating natural frequencies of isotropic plates as well as their lateral deflection under uniform loading [64,65]. The effects of different geometrical parameters, boundary conditions, and material properties on an isotropic plate's natural frequency and lateral deflection have been well established [66,67]. Due to the complex shapes of auxetic materials, computational methods are primarily used in the literature to characterize the behavior of auxetic structures [68–70]. The dynamic and static response of auxetic plates has been investigated by using finite element analysis (FEA) [71–74].

In this study, the effect of design parameters on the mechanical properties and auxetic behavior of bi-material non-porous plates is investigated; then, finite element simulation is employed to determine the natural frequency of the architected plates and their lateral deflection under static loading. Moreover, the accuracy of the homogenization technique in the prediction of dynamic and static responses of the architected plates is investigated.

2. Materials and Methods

The NPR effect can be achieved by the rigid rotary units in 2D structures wherein internal void spaces enable the rigid units to rotate freely under loading conditions, as illustrated in Figure 1. After rotation, void spaces between the rigid units significantly alter their shapes, and as a result, the area of the unit cells decreases, which can produce an NPR effect.

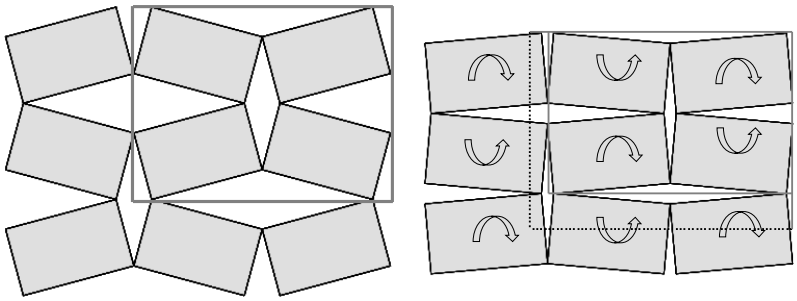

(**a**) (**b**)

Figure 1. Illustration of the rotation mechanism of 2D structure with rotating unit cells, which creates NPR effect. Rigid units (**a**) before rotation and (**b**) after rotation.

Similarly, a plate comprises a hard matrix, and soft inclusions can offer an NPR effect. A unit cell that includes a hard matrix and soft diamond shape inclusions is shown in Figure 2. Both matrix and inclusions are isotropic elastic materials.

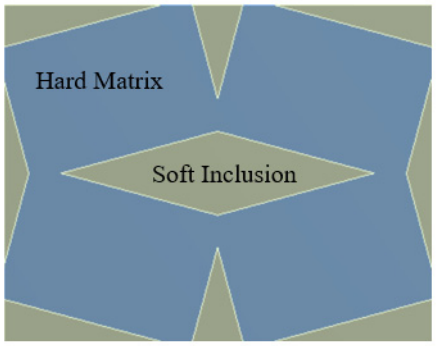

Figure 2. The unit cell comprises a hard matrix and soft inclusions.

Multi-material additive manufacturing is one of the techniques that can be employed to create architected bi-material plates [63,75]. Matrix and inclusions should be selected from materials that develop a strong adhesion to each other [76,77]. Figure 3 shows an example of an architected plate fabricated by multi-material additive manufacturing. The hard matrix is from carbon fiber reinforced PLA, and the soft inclusions are from PLA.

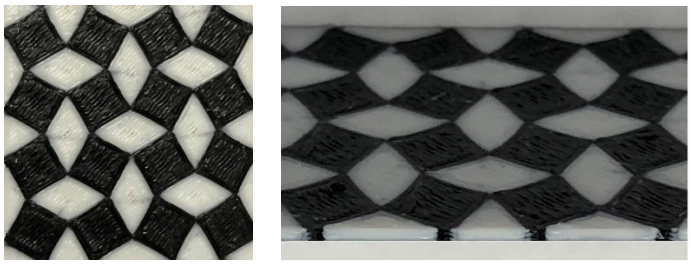

(**a**) (**b**)

Figure 3. Architected plate fabricated by multi-material additive manufacturing: (**a**) top view (**b**) inclined view.

In practice, plates having a finite thickness will tend to deform out of plane under compression, a phenomenon that will affect the Poisson's ratio in the plane. Therefore, the plate needs to have a considerable thickness to work effectively. In this regard, the scope of this study is limited to the design and computational analysis of architected bi-material plates.

Poisson's ratio and Young's modulus of architected bi-material auxetic plates can be determined by finite element analysis. The finite element analysis was performed using Ansys 2019 version (ANSYS Inc., Canonsburg, PA, USA), and 3D solid tetrahedral and hexahedral elements with quadratic element order were used to mesh the architected plates in this study. The length and width of the architected plate are L and L', as shown in Figure 4a. The left side of the plate is fixed, and a longitudinal deformation of δ is applied on the right side of the plate, as shown in Figure 4b. The maximum total lateral deformation, δ', is determined from finite element simulation. Therefore, the strains along the length of the plate, ε, and along the width, ε', are defined as

$$\varepsilon = \frac{\delta}{L} \qquad \varepsilon\prime = -\frac{\delta\prime}{L\prime} \tag{1}$$

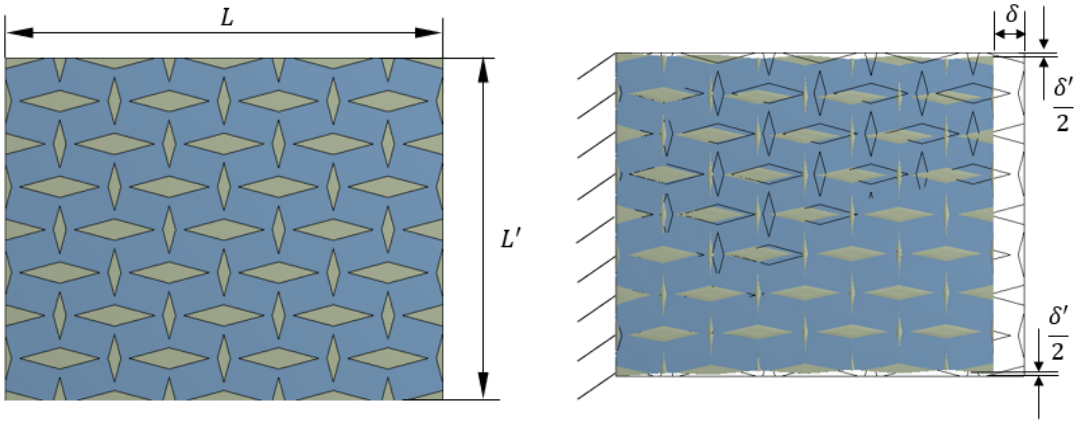

(**a**) (**b**)

Figure 4. (**a**) Architected plate with rotating rigid units; (**b**) illustration of the NPR effect.

The Poisson's ratio v is determined as

$$v = -\frac{\varepsilon\prime}{\varepsilon} \tag{2}$$

The auxetic behavior of the architected plate can be observed in Figure 4b.

In order to find Young's modulus of the plate, E, first, the reaction force, F, on the left (fixed) side of the plate is determined from finite element simulation. The amount of stress σ developed in the plate with the lateral cross-sectional area of A is determined as

$$\sigma = \frac{F}{A} \tag{3}$$

Then, Young's modulus is obtained as

$$E = \frac{\sigma}{\varepsilon} \tag{4}$$

It should be noted that each unit cell, as shown in Figure 2, is a representative unit of the architected plate.

The angular frequencies, ω_n, of an isotropic elastic square plate with clamped edges are given as [66]

$$\omega_n = 2\pi f_n = k_n \left[\frac{Et^2}{\rho L^4(1-v^2)}\right]^{0.5}, \; k_1 = 10.40, \; k_2 = 21.21, k_3 = 31.29, \tag{5}$$

where f_n are natural frequencies, E is Young's modulus, v is the Poisson's ratio, n is a mode of vibration, ρ is density, L is the length of the sides of the plate, and t is the plate thickness.

The lateral deflection at the center of an isotropic elastic rectangular plate under uniform lateral loading, as shown in Figure 5, is [67]

$$W_{x=0,\; y=0} = \alpha \frac{pb^4}{D} \tag{6}$$

where α is a constant depending on (b/a) and Poisson's ratio, b and a are half the length and width of the plate ($a \geq b$), p is the intensity of lateral pressure, and D is the constant flexural rigidity defined as

$$D = \frac{Et^3}{12(1-v^2)} \tag{7}$$

where E is Young's modulus, v is the Poisson's ratio, and t is the plate thickness.

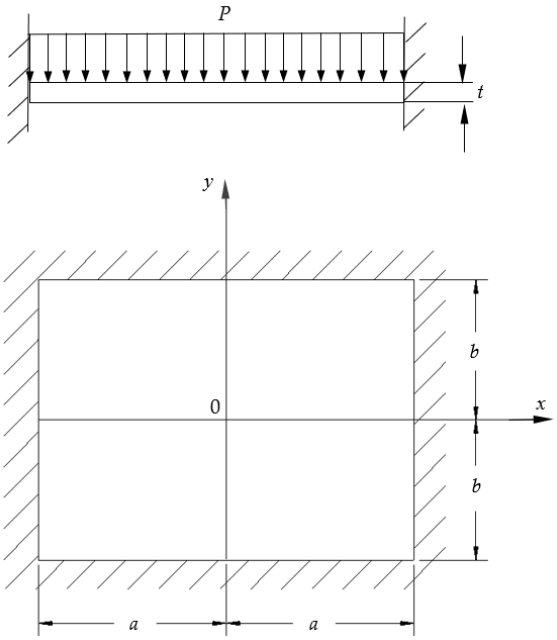

Figure 5. An isotropic elastic rectangular plate with clamped edges under lateral pressure.

3. Results and Discussion

3.1. Effect of Design Parameters on Mechanical Properties

The design parameters of unit cells may significantly change the mechanical properties of the architected bi-material plate. a, s, θ, g, and t are defined as geometric design parameters of the cellular structure with diamond shape inclusions, as shown in Figure 6. t is the thickness of the unit cell.

The ratio of Young's modulus of the soft inclusions, E_s, to Young's modulus of the hard matrix, E_h, introduces another design parameter, λ, defined as

$$\lambda = \frac{E_s}{E_h} \tag{8}$$

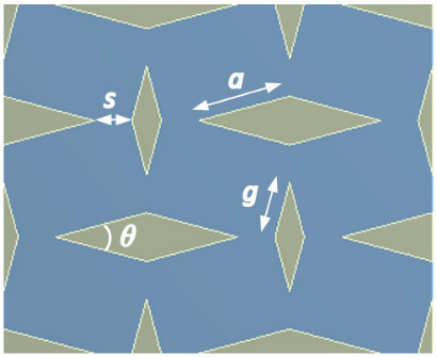

Figure 6. Geometric design parameters of the cellular structure with diamond shape inclusions.

For example, the geometric design parameters can be taken as $a = g = 5$ mm, s = $t = 1$ mm, $\theta = 30°$, which yields the plate side length of $L = L' = 56.99$ mm. Young's modulus of hard and soft materials can be taken as $E_h = 1$ GPa, $E_s = 0.01$ GPa, which yields $\lambda = 0.01$. Both the hard matrix and soft inclusions have the Poisson's ratio of 0.25. By applying $\delta = 1$ mm, as shown in Figure 4, δ' is computed as 0.473 mm, which yields the Poisson's ratio of $v = -0.473$. The area at the fixed end is $A = 56.99$ mm^2. The reaction force at the fixed end is computed as $F = 184.76$ N, which creates longitudinal stress of $\sigma = 3.24$ MPa in the plate. The longitudinal strain in the plate is $\varepsilon = 0.01754$. Therefore, Young's modulus of the plate is $E = 184.76$ MPa.

In this study, dimensionless values are used. Here, E_h takes the value of 1, and both the hard matrix and soft inclusions have the same Poisson's ratio ($v_h = v_s = 0.25$). The effects of design parameters on Poisson's ratio and Young's modulus of the bi-material plate are given in Figure 7a–e. In Figure 7a, θ is a variable ($2.5° \leq \theta \leq 90°$), and other design parameters are set to $a = g = 5$, $s = t = 1$, and $\lambda = 0.01$. The Poisson's ratio and Young's modulus reach their minimum values of -0.47 and 0.18, respectively, at $\theta = 30°$. In Figure 7b, g is a variable ($0.1 \leq g \leq 5$), and other parameters are set to $a = 5$, $s = t = 1$, $\theta = 30°$, and $\lambda = 0.01$. The Poisson's ratio reaches its minimum value of -0.54 at $g = 4$. The Young's modulus reaches its maximum value of 0.53 at $g = 1.5$. In Figure 7c, s is a variable ($0.1 \leq s \leq 8$), and other parameters are set to $a = g = 5$, $\theta = 30°$, $t = 1$, and $\lambda = 0.01$. The Poisson's ratio and Young's modulus obtain their minimum values of -0.52 and 0.1 at the smallest value of s (i.e., $s = 0.1$). In Figure 7d, t is a variable ($0.1 \leq t \leq 6$), and other design parameters are set to $a = g = 5$, $s = 1$, and $\lambda = 0.01$. It can be seen that the variation of the plate thickness has a relatively small effect on the Poisson's ratio and Young's modulus of the plate. The Poisson's ratio and Young's modulus obtain their minimum values of -0.476 and 0.183 at the smallest value of t (i.e., $t = 0.1$).

In Figure 7e, λ is a variable ($0.00001 \leq \lambda \leq 1$), and other parameters are set to $a = g = 5$, $s = t = 1$, and $\theta = 30°$. The Poisson's ratio and Young's modulus obtain their minimum values of -0.92 and 0.08 at the smallest value of λ (i.e., $\lambda = 0.00001$). This shows that having porosity instead of soft inclusions increases the auxetic behavior of the plate and yields a more flexible plate. The Poisson's ratio obtains a zero value at $\lambda = 0.058$.

Depending on the application of the plate, the design parameters can be adjusted to render a specific mechanical property. It can be observed that only by changing the geometric design parameters, the Poisson's ratio with a range of -0.54 to 0.78 and Young's modulus with a range of 0.10 to 0.69 are produced merely by the use of two distinct materials with certain moduli (i.e., $E_h = 1$, $E_s = 0.01$) and the same Poisson's ratio ($v = 0.25$). This is significant because we can create a variety of mechanical properties for plates with a limited number of materials.

3.2. Effect of Design Parameters on Dynamic Response

In order to investigate the dynamic response of the bi-material architected plate, λ was selected as a variable, while geometric design parameters were taken as constants; $a = g = 5$, $s = t = 1$, and $\theta = 30°$. The variation in the non-geometric design parameter λ does not alter the size of the plate, and the plate keeps its square shape with the same

number of inclusions, as shown in Figure 8a. The first three mode shapes of vibration of the architected plate with clamped boundary conditions are presented in Figure 8b–d. It can be observed that the plate shows the same mode shapes of vibration as a homogenous rectangular plate, though with different natural frequencies.

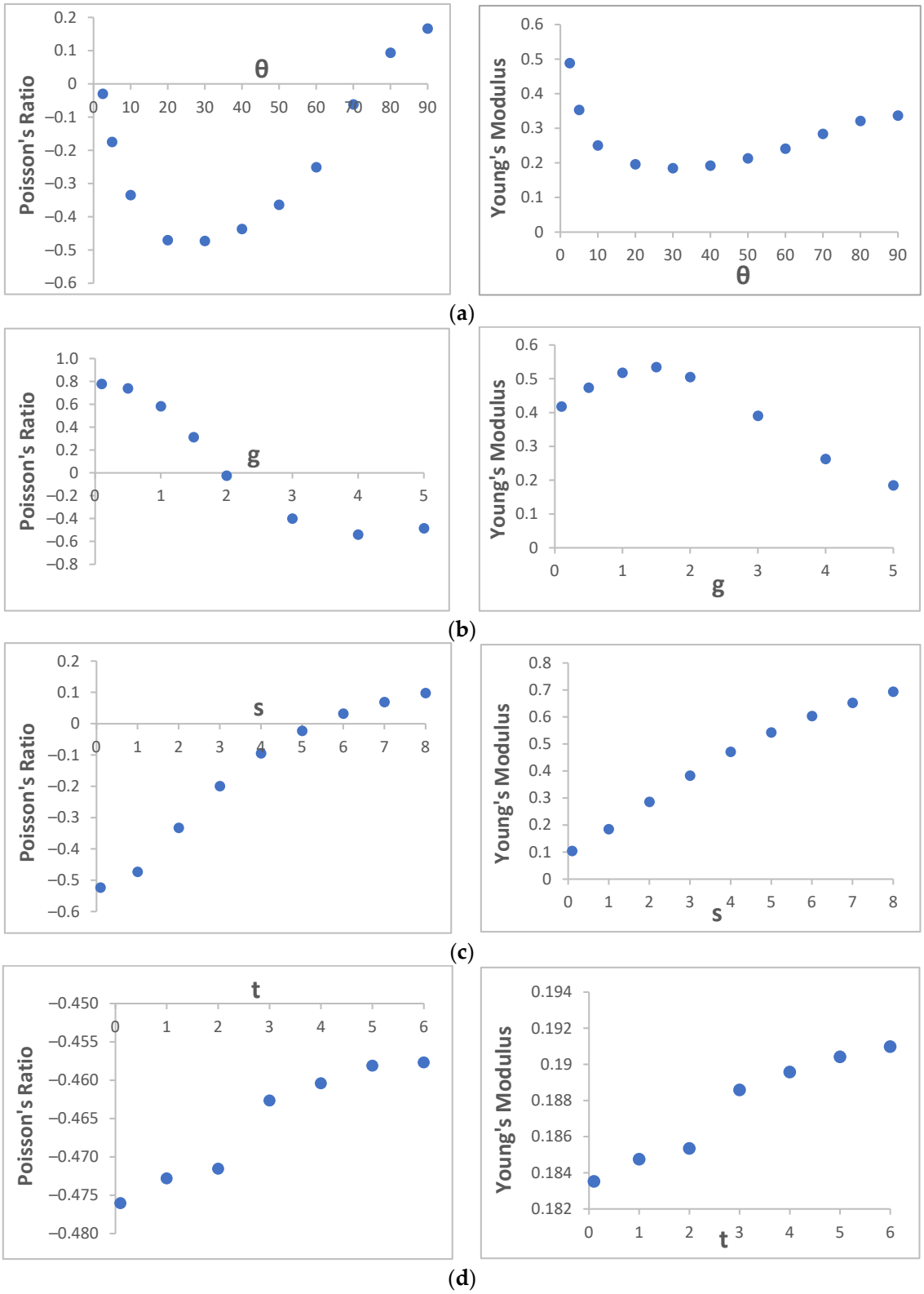

Figure 7. *Cont.*

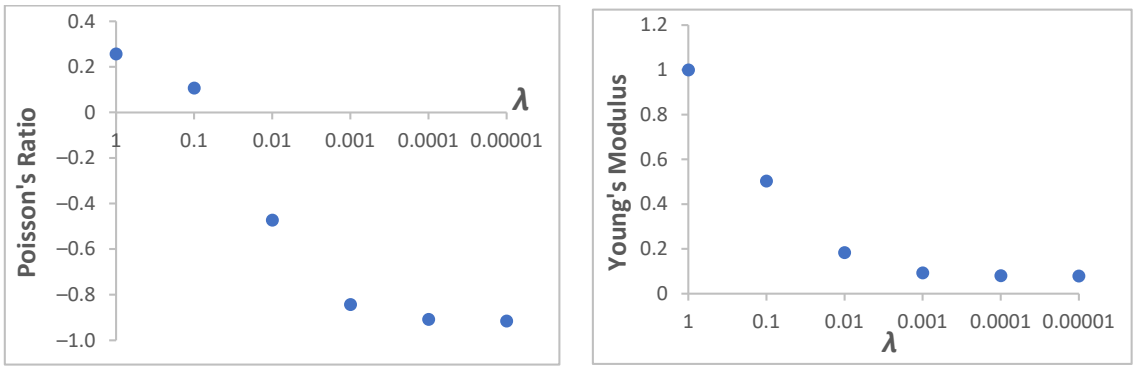

(**e**)

Figure 7. Effects of design parameters (**a**) θ, (**b**) g, (**c**) s, (**d**) t, and (**e**) λ on Poisson's ratio and Young's modulus of the bi-material plate.

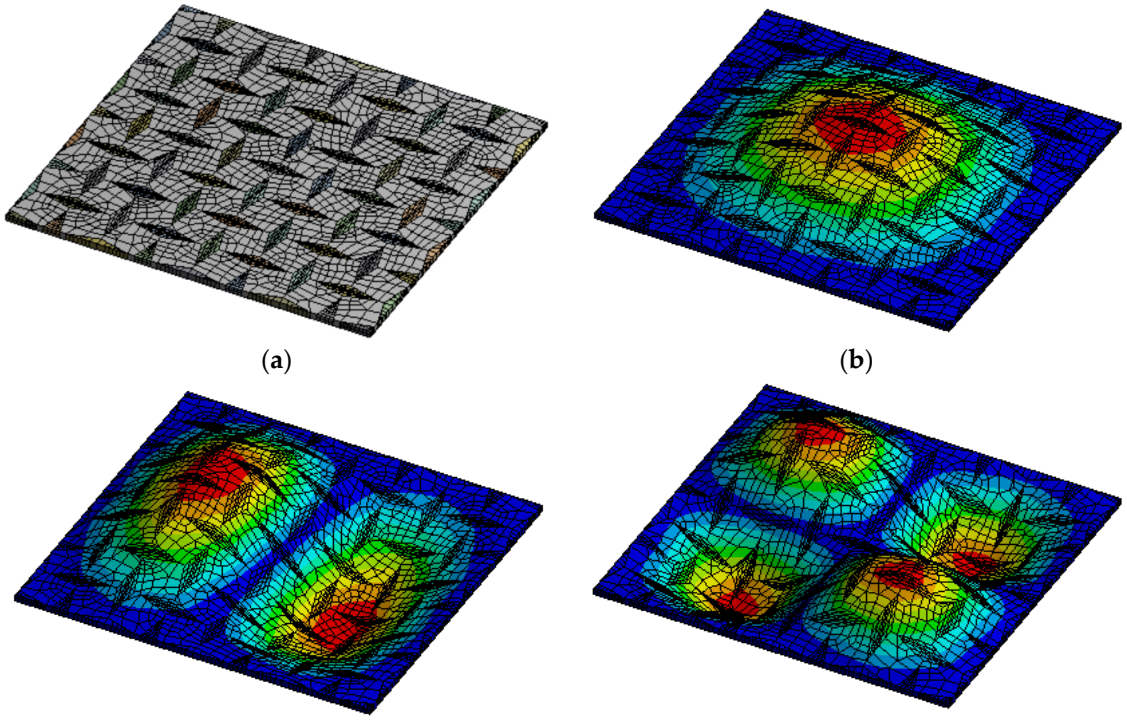

(**a**) (**b**)

(**c**) (**d**)

Figure 8. Mode shapes of vibration of the architected plate with clamped boundary conditions obtained by finite element analysis. (**a**) The undeformed plate; the (**b**) first, (**c**) second, and (**d**) third mode of vibration.

Figure 9 presents the natural frequencies of the first three modes of vibration of the architected plate with different values of λ. All frequencies are normalized to the first natural frequency of the plate with $\lambda = 1$. It is assumed that both the hard matrix and soft inclusions have the same density ($\rho_h = \rho_s$). For example, the first natural frequency for the homogenous plate (i.e., $\lambda = 1$) with $E_h = E_s = 1$ GPa, $v_h = v_s = 0.25$, $\rho_h = \rho_s = 1000$ kg/m^3, $a = g = 5$ mm, s = $t = 1$ mm, and $\theta = 30^\circ$ is 526.34 Hz, which is the frequency that all frequencies are normalized to in the chart. It can be observed that by reducing λ, the natural frequencies decrease as well.

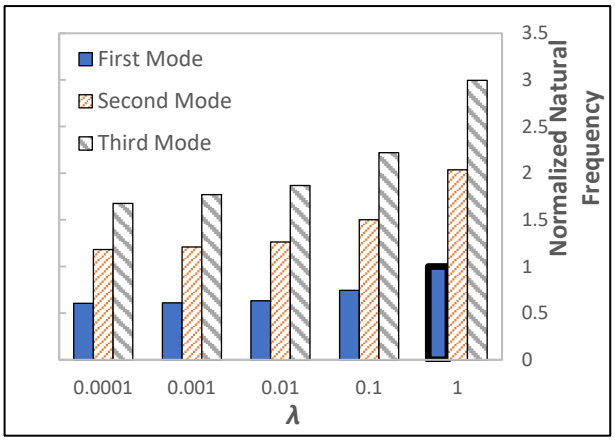

Figure 9. Natural frequencies of the first three modes of vibration of the architected plate. All frequencies are normalized to the first natural frequency of the plate with $\lambda = 1$ (the bar with a thick borderline on the chart).

Figure 10 presents the natural frequencies of the first three modes of vibration that are normalized to the natural frequency of the plate with $\lambda = 1$ of the corresponding vibration mode. The comparison of these natural frequencies to the natural frequencies of a homogenized plate is also given in Figure 10. The natural frequencies of a homogenized plate were calculated based on Equation (5), using the Young's modulus and Poisson's ratio that were obtained from finite element analysis of the architected plate at each λ. The natural frequencies of a homogenized plate are then normalized to the natural frequency of the plate with $\lambda = 1$ of the corresponding vibration mode, which gives the same value at each λ for all modes of vibration, as can be seen in Figure 10.

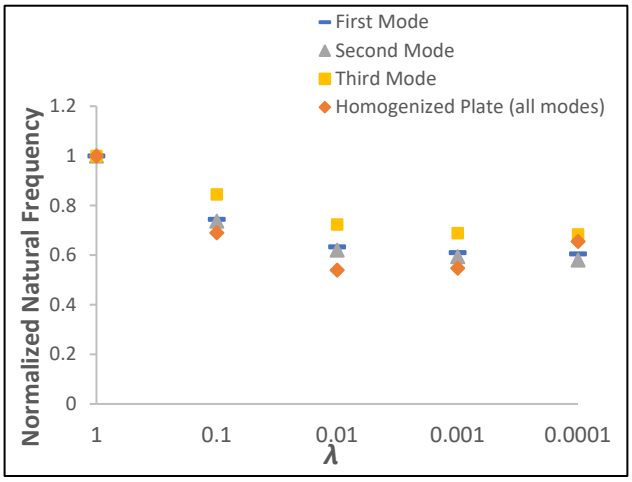

Figure 10. Effects of Young's modulus ratio, λ, on natural frequencies of the bi-material plate. $a = g = 5$, $s = t = 1$, $\theta = 30°$. Frequencies are normalized to the natural frequency of the plate with $\lambda = 1$ for the corresponding vibration mode.

According to Equation (5), the natural frequencies of an isotropic homogeneous square plate depend on its Young's modulus and Poisson's ratio, which vary by the change in the design parameter λ, as demonstrated in Figure 7e. It can be observed that the homogenization technique provides a good estimate of natural frequencies, primarily for the first and second modes of vibration.

3.3. Effect of Design Parameters on Static Response

For evaluation of the static response of the architected plate, similarly to the dynamic response analysis, λ was selected as a variable, while geometric design parameters were

taken as constants; $a = g = 5$, $s = t = 1$, and $\theta = 30°$. The deformation of the architected plate under uniform lateral loading with clamped edges is shown in Figure 11. It can be observed that the maximum deflection occurs at the center of the plate.

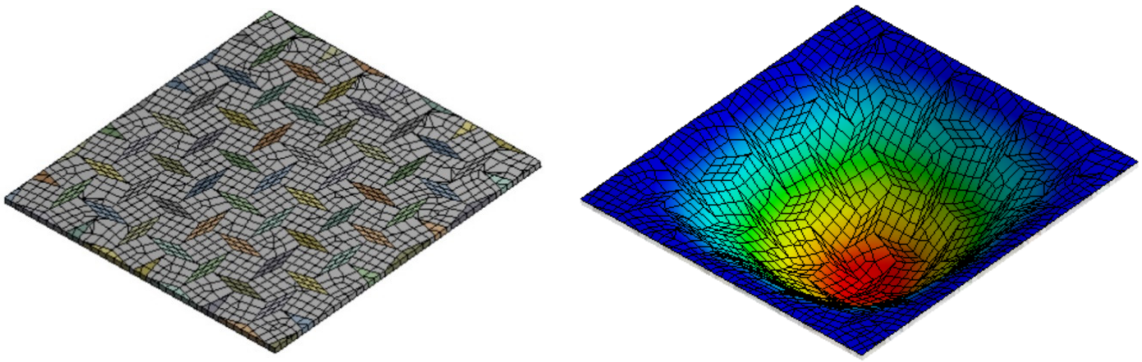

(**a**) (**b**)

Figure 11. Finite element model of (**a**) undeformed architected plate and (**b**) deformed architected plate under uniform lateral loading.

Figure 12 presents the lateral deflection at the center of the architected plate under lateral pressure that is normalized to the lateral deflection of the center of a plate with $\lambda = 1$ under the same loading condition. As stated in Equation (6), the lateral deflection of an isotropic homogeneous rectangular plate under lateral pressure depends on its Young's modulus and Poisson's ratio, which vary by the change in λ. The comparison of the results to the lateral deflection at the center of an isotropic elastic rectangular plate with the same Young's modulus and Poisson's ratio is also presented in Figure 12. As shown in the dynamic response, the homogenization technique provides a reasonable estimate for the static response of the architected plate over the high and low range of λ. Contrarily, it gives a poor estimate for λ values in between, as demonstrated in Figure 12. This is due to the fact that under direct loading, soft inclusions cannot freely deform, as they are bounded by the hard matrix. However, this condition does not apply to the equivalent homogenized plate, and therefore, a larger deformation can be observed. The effect of this condition decreases when the inclusions are made of harder materials, or they can be considered porosity when they are extremely soft.

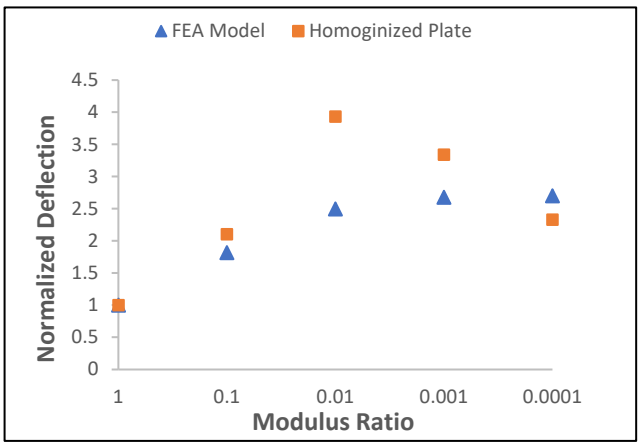

Figure 12. Effects of Young's modulus ratio, λ, on the lateral deflection at the center of the bi-material architected plate under lateral pressure. $a = g = 5$, $s = t = 1$, $\theta = 30°$. Deflections are normalized to the lateral deflection of the center of a plate with $\lambda = 1$.

4. Conclusions

In this study, a non-porous auxetic plate was developed by embedding soft diamond shape inclusions within the hard matrix. It was shown that a variety of mechanical prop-

erties, such as different levels of Young's modulus and negative Poisson's ratio, could be achieved by changing the geometric design parameters of cellular structures. It was observed that the Poisson's ratio with a range of −0.54 to 0.78 and Young's modulus with a range of 0.10 to 0.69 were produced by only the use of two unique materials with certain moduli (i.e., $E_h = 1$, $E_s = 0.01$) and the same Poisson's ratio ($v = 0.25$). Furthermore, the effect of Young's modulus ratio, λ, as a design parameter on the mechanical properties of the architected plate and its natural frequencies with clamped boundary conditions as well as its deflection under uniform lateral loading were presented. Soft inclusions reduced the auxetic behavior of the architected plate as compared to porosities. It was demonstrated that the homogenization technique based on the mechanical properties obtained by finite element analysis could well estimate the architected plate's dynamic response for different λ values, specifically for the first and second modes of vibration. The homogenization technique also provides a reasonable estimate of the static response over the high and low range of λ.

Author Contributions: Conceptualization, A.A.; Software, A.A. and H.R.; Investigation, H.R.; Methodology, A.A. and H.R.; Supervision, A.A.; Writing—original draft, A.A. and H.R.; Writing—review and editing, A.A. All authors have read and agreed to the published version of the manuscript.

Funding: This research received no external funding.

Institutional Review Board Statement: Not applicable.

Informed Consent Statement: Not applicable.

Data Availability Statement: The data presented in this study are available on request from the corresponding author.

Acknowledgments: The authors would like to thank Provost Office at Mercer University for supporting this work through the SEED grant program.

Conflicts of Interest: The authors declare no conflict of interest.

References

1. Landau, L.D.; Lifshitz, E.M. *Theory of Elasticity*, 3rd ed.; Elsevier: Amsterdam, The Netherlands, 1986; Volume 7.
2. Carneiro, V.H.; Meireles, J.; Puga, H. Auxetic materials—A review. *Mater. Sci.-Pol.* **2013**, *31*, 561–571. [CrossRef]
3. Evans, K.E.; Nkansah, M.A.; Hutchinson, I.J. Auxetic foams: Modelling negative Poisson's ratios. *Acta Metall. Mater.* **1994**, *42*, 1289–1294. [CrossRef]
4. Evans, K.E. Auxetic polymers: A new range of materials. *Endeavour* **1991**, *15*, 170–174. [CrossRef]
5. Love, A.E.H. *A Treatise on the Mathematical Theory of Elasticity*, 4th ed.; Cambridge University Press: Cambridge, UK, 1944.
6. Saxena, K.K.; Das, R.; Calius, E.P. Three Decades of Auxetics Research—Materials with Negative Poisson's Ratio: A Review. *Adv. Eng. Mater.* **2016**, *18*, 1847–1870. [CrossRef]
7. Lakes, R. Foam structures with a negative poisson's ratio. *Science* **1987**, *235*, 1038–1040. [CrossRef]
8. Duncan, O.; Shepherd, T.; Moroney, C.; Foster, L.; Venkatraman, P.D.; Winwood, K.; Allen, T.; Alderson, A. Review of auxetic materials for sports applications: Expanding options in comfort and protection. *Appl. Sci. (Switz.)* **2018**, *8*, 941. [CrossRef]
9. Yang, C.; Vora, H.D.; Chang, Y. Behavior of auxetic structures under compression and impact forces. *Smart Mater. Struct.* **2018**, *27*, 025012. [CrossRef]
10. Scarpa, F.; Ciffo, L.G.; Yates, J.R. Dynamic properties of high structural integrity auxetic open cell foam. *Smart Mater. Struct.* **2004**, *13*, 49. [CrossRef]
11. Hou, Y.; Neville, R.; Scarpa, F.; Remillat, C.; Gu, B.; Ruzzene, M. Graded conventional-auxetic Kirigami sandwich structures: Flatwise compression and edgewise loading. *Compos. Part B Eng.* **2014**, *59*, 33–42. [CrossRef]
12. Milton, G.W. Composite materials with poisson's ratios close to—1. *J. Mech. Phys. Solids* **1992**, *40*, 1105–1137. [CrossRef]
13. Alderson, K.L.; Evans, K.E. The fabrication of microporous polyethylene having a negative Poisson's ratio. *Polymer (Guildf)* **1992**, *33*, 4435–4438. [CrossRef]
14. Caddock, B.D.; Evans, K.E. Microporous materials with negative Poisson's ratios. I. Microstructure and mechanical properties. *J. Phys. D Appl. Phys.* **1989**, *22*, 1877. [CrossRef]
15. Masters, I.G.; Evans, K.E. Models for the elastic deformation of honeycombs. *Compos. Struct.* **1996**, *35*, 403–422. [CrossRef]
16. Kimizuka, H.; Kaburaki, H.; Kogure, Y. Mechanism for negative poisson ratios over the α-β transition of cristobalite, SiO_2: A molecular-dynamics study. *Phys. Rev. Lett.* **2000**, *84*, 5548. [CrossRef]

17. Baughman, R.H.; Shacklette, J.M.; Zakhidov, A.A.; Stafström, S. Negative poisson's ratios as a common feature of cubic metals. *Nature* **1998**, *392*, 362–365. [CrossRef]
18. Grima, J.N.; Winczewski, S.; Mizzi, L.; Grech, M.C.; Cauchi, R.; Gatt, R.; Attard, D.; Wojciechowski, K.W.; Rybicki, J. Tailoring graphene to achieve negative poisson's ratio properties. *Adv. Mater.* **2015**, *27*, 1455–1459. [CrossRef]
19. Wojciechowski, K.W. Constant thermodynamic tension monte carlo studies of elastic properties of a two-dimensional system of hard cyclic hexamers. *Mol. Phys.* **1987**, *61*, 1247–1258. [CrossRef]
20. Wojciechowski, K.W. Two-dimensional isotropic system with a negative poisson ratio. *Phys. Lett. A* **1989**, *137*, 60–64. [CrossRef]
21. Brańka, A.C.; Heyes, D.M.; Wojciechowski, K.W. Auxeticity of cubic materials. *Phys. Status Solidi (B) Basic Res.* **2009**, *246*, 2063–2071. [CrossRef]
22. Ting, T.C.T.; Barnett, D.M. Negative poisson's ratios in anisotropic linear elastic media. *J. Appl. Mech. Trans. ASME* **2005**, *72*, 929–931. [CrossRef]
23. Grima, J.N.; Wojciechowski, K.W. Preface: Phys. stat. sol. (b) 245/11. *Phys. Status Solidi (B)* **2008**, *245*, 2369–2372. [CrossRef]
24. Brańka, A.C.; Heyes, D.M.; Maćkowiak, S.; Pieprzyk, S.; Wojciechowski, K.W. Cubic materials in different auxetic regions: Linking microscopic to macroscopic formulations. *Phys. Status Solidi (B) Basic Res.* **2012**, *249*, 1373–1378. [CrossRef]
25. Robert, F. An isotropic three-dimensional structure with Poisson's ratio = −1. *J. Elast.* **1985**, *15*, 427–430. [CrossRef]
26. Alderson, K.L.; Fitzgerald, A.; Evans, K.E. The strain dependent indentation resilience of auxetic microporous polyethylene. *J. Mater. Sci.* **2000**, *35*, 4039–4047. [CrossRef]
27. Evans, K.E.; Alderson, A. Auxetic materials: Functional materials and structures from lateral thinking! *Adv. Mater.* **2000**, *12*, 617–628. [CrossRef]
28. Peliński, K.; Smardzewski, J.; Narojczyk, J. Stiffness of Synclastic Wood-Based Auxetic Sandwich Panels. *Phys. Status Solidi (B) Basic Res.* **2020**, *257*, 1900749. [CrossRef]
29. Choi, J.B. Fracture toughness of re-entrant foam materials with a negative Poisson's ratio: Experiment and analysis. *Int. J. Fract.* **1996**, *80*, 73–83. [CrossRef]
30. Scarpa, F.; Bullough, W.A.; Lumley, P. Trends in acoustic properties of iron particle seeded auxetic polyurethane foam. *Proc. Inst. Mech. Eng. Part C J. Mech. Eng. Sci.* **2004**, *218*, 241–244. [CrossRef]
31. Howell, B.; Prendergast, P.; Hansen, L. Examination of acoustic behavior of negative poisson's ratio materials. *Appl. Acoust.* **1994**, *43*, 141–148. [CrossRef]
32. Scarpa, F.; Yates, J.R.; Ciffo, L.G.; Patsias, S. Dynamic crushing of auxetic open-cell polyurethane foam. *Proc. Inst. Mech. Eng. Part C J. Mech. Eng. Sci.* **2002**, *216*, 1153–1156. [CrossRef]
33. Imbalzano, G.; Tran, P.; Ngo, T.D.; Lee, P.V.S. Three-dimensional modelling of auxetic sandwich panels for localised impact resistance. *J. Sandw. Struct. Mater.* **2017**, *19*, 291–316. [CrossRef]
34. Wu, W.; Xiao, D.; Meng, J.; Liu, K.; Niu, Y.; Xue, R.; Zhang, P.; Ding, W.; Ye, X.; Ling, X.; et al. Mechanical design, impact energy absorption and applications of auxetic structures in automobile lightweight engineering. *Lixue Xuebao/Chin. J. Theor. Appl. Mech.* **2021**, *53*, 611–638. [CrossRef]
35. Ren, X.; Zhang, X.; Xie, Y. Research Progress in Auxetic Materials and Structures. *Lixue Xuebao/Chin. J. Theor. Appl. Mech.* **2019**, *51*, 656–689. [CrossRef]
36. Chan, N.; Evans, K.E. Fabrication methods for auxetic foams. *J. Mater. Sci.* **1997**, *32*, 5945–5953. [CrossRef]
37. Alderson, A.; Alderson, K.L.; Chirima, G.; Ravirala, N.; Zied, K.M. The in-plane linear elastic constants and out-of-plane bending of 3-coordinated ligament and cylinder-ligament honeycombs. *Compos. Sci. Technol.* **2010**, *70*, 1034–1041. [CrossRef]
38. Gaspar, N.; Smith, C.W.; Alderson, A.; Grima, J.N.; Evans, K.E. A generalised three-dimensional tethered-nodule model for auxetic materials. *J. Mater. Sci.* **2011**, *46*, 372–384. [CrossRef]
39. Cho, H.; Seo, D.; Kim, D.N. Mechanics of auxetic materials. In *Handbook of Mechanics of Materials*; Springer: Berlin/Heidelberg, Germany, 2019. [CrossRef]
40. Grima, J.N.; Alderson, A.; Evans, K.E. Auxetic behaviour from rotating rigid units. *Phys. Status Solidi (B) Basic Res.* **2005**, *242*, 561–575. [CrossRef]
41. Grima, J.N.; Evans, K.E. Auxetic behavior from rotating squares. *J. Mater. Sci. Lett.* **2000**, *19*, 1563–1565. [CrossRef]
42. Attard, D.; Grima, J.N. Auxetic behaviour from rotating rhombi. *Phys. Status Solidi (B) Basic Res.* **2008**, *245*, 2395–2404. [CrossRef]
43. Poźniak, A.A.; Wojciechowski, K.W.; Grima, J.N.; Mizzi, L. Planar auxeticity from elliptic inclusions. *Compos. Part B Eng.* **2016**, *94*, 379–388. [CrossRef]
44. Ishibashi, Y.; Iwata, M. A microscopic model of a negative Poisson's ratio in some crystals. *J. Phys. Soc. Jpn.* **2000**, *69*, 2702–2703. [CrossRef]
45. Dubrovski, P.D.; Novak, N.; Borovinšek, M.; Vesenjak, M.; Ren, Z. In-Plane Deformation Behavior and the Open Area of Rotating Squares in an Auxetic Compound Fabric. *Polymers (Basel)* **2022**, *14*, 571. [CrossRef] [PubMed]
46. Hou, X.; Hu, H.; Silberschmidt, V. A novel concept to develop composite structures with isotropic negative Poisson's ratio: Effects of random inclusions. *Compos. Sci. Technol.* **2012**, *72*, 1848–1854. [CrossRef]
47. Grima, J.N.; Gatt, R. Perforated sheets exhibiting negative Poisson's ratios. *Adv. Eng. Mater.* **2010**, *12*, 460–464. [CrossRef]
48. Tretiakov, K.V. Negative Poisson's ratio of two-dimensional hard cyclic tetramers. *J. Non-Cryst. Solids* **2009**, *355*, 1435–1438. [CrossRef]

49. Tretiakov, K.V.; Wojciechowski, K.W. Auxetic, Partially Auxetic, and Nonauxetic Behaviour in 2D Crystals of Hard Cyclic Tetramers. *Phys. Status Solidi—Rapid Res. Lett.* **2020**, *14*, 2000198. [CrossRef]
50. Nazir, A.; bin Arshad, A.; Jeng, J.Y. Buckling and post-buckling behavior of uniform and variable-density lattice columns fabricated using additive manufacturing. *Materials* **2019**, *12*, 3539. [CrossRef]
51. Nazir, A.; bin Arshad, A.; Hsu, C.P.; Jeng, J.Y. Effect of fillets on mechanical properties of lattice structures fabricated using multi-jet fusion technology. *Materials* **2021**, *14*, 2194. [CrossRef]
52. bin Arshad, A.; Nazir, A.; Jeng, J.Y. Design and performance evaluation of multi-helical springs fabricated by Multi Jet Fusion additive manufacturing technology. *Int. J. Adv. Manuf. Technol.* **2022**, *118*, 195–206. [CrossRef]
53. Velásquez, M.B.; Francesconi, L.; Taylor, M. Design of low-porosity auxetic tessellations with reduced mechanical stress concentrations. *Extrem. Mech. Lett.* **2021**, *48*, 101401. [CrossRef]
54. Meena, K.; Singamneni, S. A new auxetic structure with significantly reduced stress concentration effects. *Mater. Des.* **2019**, *173*, 107779. [CrossRef]
55. Afshar, A.; Alkhader, M.; Korach, C.S.; Chiang, F.P. Effect of long-term exposure to marine environments on the flexural properties of carbon fiber vinylester composites. *Compos. Struct.* **2015**, *126*, 72–77. [CrossRef]
56. Afshar, A.; Mihut, D.; Chen, P. Effects of environmental exposures on carbon fiber epoxy composites protected by metallic thin films. *J. Compos. Mater.* **2020**, *54*, 167–177. [CrossRef]
57. Afshar, A.; Mihut, D.; Hill, S.; Baqersad, J. Synergistic effects of environmental exposures on polymer matrix with or without metallic coating protection. *J. Compos. Mater.* **2018**, *52*, 3773–3784. [CrossRef]
58. Afshar, A.; Liao, H.T.; pen Chiang, F.; Korach, C.S. Time-dependent changes in mechanical properties of carbon fiber vinyl ester composites exposed to marine environments. *Compos. Struct.* **2016**, *144*, 80–85. [CrossRef]
59. Tan, H.; Yu, L.; Zhou, Z. Negative Poisson's ratio in non-porous smooth curve sheet. *Phys. Status Solidi (B) Basic Res.* **2017**, *254*, 1600612. [CrossRef]
60. Javid, F.; Smith-Roberge, E.; Innes, M.C.; Shanian, A.J.; Weaver, C.; Bertoldi, K. Dimpled elastic sheets: A new class of non-porous negative Poisson's ratio materials. *Sci. Rep.* **2015**, *5*, 18373. [CrossRef]
61. Schwerdtfeger, J.; Heinl, P.; Singer, R.F.; Körner, C. Auxetic cellular structures through selective electron-beam melting. *Phys. Status Solidi (B) Basic Res.* **2010**, *247*, 269–272. [CrossRef]
62. Dudte, L.H.; Vouga, E.; Tachi, T.; Mahadevan, L. Programming curvature using origami tessellations. *Nat. Mater.* **2016**, *15*, 583–588. [CrossRef]
63. Ngo, T.D.; Kashani, A.; Imbalzano, G.; Nguyen, K.T.Q.; Hui, D. Additive manufacturing (3D printing): A review of materials, methods, applications and challenges. *Compos. Part B Eng.* **2018**, *143*, 172–196. [CrossRef]
64. Gharaibeh, M.A.; Obeidat, A.M. Vibrations analysis of rectangular plates with clamped corners. *Open Eng.* **2018**, *8*, 275–283. [CrossRef]
65. Imrak, C.E.; Gerdemeli, I. The problem of isotropic rectangular plate with four clamped edges. *Sadhana—Acad. Proc. Eng. Sci.* **2007**, *32*, 181–186. [CrossRef]
66. Hearmon, R.F.S. The Frequency of Vibration of Rectangular Isotropic Plates. *J. Appl. Mech.* **1952**, *19*, 402–403. [CrossRef]
67. İmrak, C.E.; Gerdemeli, İ. An Exact Solution for the Deflection of a Clamped Rectangular Plate Under Uniform load. *Appl. Math. Sci.* **2007**, *1*, 2129–2137.
68. Pozniak, A.A.; Smardzewski, J.; Wojciechowski, K.W. Computer simulations of auxetic foams in two dimensions. *Smart Mater. Struct.* **2013**, *22*, 084009. [CrossRef]
69. Hoover, W.G.; Hoover, C.G. Searching for auxetics with DYNA3D and ParaDyn. *Phys. Status Solidi (B) Basic Res.* **2005**, *242*, 585–594. [CrossRef]
70. Strek, T.; Kedziora, P.; Maruszewski, B.; Pozniak, A.A.; Tretiakov, K.V.; Wojciechowski, K.W. Finite element analysis of auxetic obstacle deformation and fluid flow in a channel. *J. Non-Cryst. Solids* **2009**, *355*, 1387–1392. [CrossRef]
71. Quoc, T.H.; Tu, T.M.; van Tham, V. Free vibration and dynamic response of sandwich composite plates with auxetic honeycomb core. *J. Sci. Technol. Civ. Eng. (STCE)—HUCE* **2021**, *15*, 1–14. [CrossRef]
72. Strek, T.; Maruszewski, B.; Narojczyk, J.W.; Wojciechowski, K.W. Finite element analysis of auxetic plate deformation. *J. Non-Cryst. Solids* **2008**, *354*, 4475–4480. [CrossRef]
73. Shilko, S.; Konyok, D. Numerical and experimental study of auxetic closed-cell foams. *Comput. Methods Sci. Technol.* **2004**, *10*, 197–202. [CrossRef]
74. Lekesiz, H.; Bhullar, S.K.; Karaca, A.A.; Jun, M.B.G. Mechanical characterization of auxetic stainless steel thin sheets with reentrant structure. *Smart Mater. Struct.* **2017**, *26*, 085022. [CrossRef]
75. Afshar, A.; Wood, R. Development of weather-resistant 3d printed structures by multi-material additive manufacturing. *J. Compos. Sci.* **2020**, *4*, 94. [CrossRef]
76. Liu, F.; Li, T.; Jiang, X.; Jia, Z.; Xu, Z.; Wang, L. The effect of material mixing on interfacial stiffness and strength of multi-material additive manufacturing. *Addit. Manuf.* **2020**, *36*, 101502. [CrossRef]
77. Afshar, A.; Mihut, D. Enhancing durability of 3D printed polymer structures by metallization. *J. Mater. Sci. Technol.* **2020**, *53*, 185–191. [CrossRef]